



**HAL**  
open science

## Absolute measurements of the double differential electronic emission cross-sections of isolated pyrene molecule (C<sub>16</sub>H<sub>10</sub>) in interaction with keV protons

Mingchao Ji, Jean-Philippe Champeaux, Patrick Moretto-Capelle, Julie Renoud, Laurent Polizzi, Stéphane Faure, Martine Sence, Pierre Cafarelli

### ► To cite this version:

Mingchao Ji, Jean-Philippe Champeaux, Patrick Moretto-Capelle, Julie Renoud, Laurent Polizzi, et al.. Absolute measurements of the double differential electronic emission cross-sections of isolated pyrene molecule (C<sub>16</sub>H<sub>10</sub>) in interaction with keV protons. *Journal of Physics B: Atomic, Molecular and Optical Physics*, 2020, 53 (22), pp.225207. 10.1088/1361-6455/abaafc . hal-03001653

**HAL Id: hal-03001653**

**<https://hal.science/hal-03001653>**

Submitted on 23 Nov 2020

**HAL** is a multi-disciplinary open access archive for the deposit and dissemination of scientific research documents, whether they are published or not. The documents may come from teaching and research institutions in France or abroad, or from public or private research centers.

L'archive ouverte pluridisciplinaire **HAL**, est destinée au dépôt et à la diffusion de documents scientifiques de niveau recherche, publiés ou non, émanant des établissements d'enseignement et de recherche français ou étrangers, des laboratoires publics ou privés.

# Absolute measurements of the double differential electronic emission cross-sections of isolated Pyrene molecule ( $C_{16}H_{10}$ ) in interaction with keV protons

M.-C. Ji<sup>1</sup>, P. Moretto-Capelle<sup>1</sup>, J. Renoud<sup>1</sup>, L. Polizzi<sup>1</sup>, S. Faure<sup>1</sup>, M. Sence<sup>1</sup>, P. Cafarelli<sup>1</sup> and J.-P. Champeaux<sup>1</sup>

<sup>1</sup>Laboratoire Collisions Agrégats et Réactivité, UMR 5589-CNRS, Université Toulouse III Paul Sabatier, 118 Route de Narbonne, 31062 Toulouse Cedex 9, France

E-mail: jean-philippe.champeaux@irsamc.ups-tlse.fr

Received xxxxxx

Accepted for publication xxxxxx

Published xxxxxx

## Abstract

Electronic emission of isolated Pyrene molecule induced by 50 to 125 keV protons has been investigated. The corresponding absolute double differential cross-sections (DDCS) have been measured at  $35^\circ$  from the incident proton beam axis. These complete measurements were compared to the simulations of emitted electrons spectra using a Semi-Classical Trajectory Monte-Carlo approach (SCTMC). The simulated SCTMC cross-sections show a reasonably good agreement with the measured ones.

Keywords: Molecular Physics, PAH, Cross Sections, Monte Carlo

---

## 1. Introduction

The polycyclic aromatic hydrocarbon (PAH) molecules are widespread from the Earth to the interstellar medium (ISM). On Earth atmosphere, the PAHs are considered as environmental pollutants, thus the studies carried on PAHs in environmental science mainly focused on their pollution, degradation and bioremediation [1], [2]. In astrophysics, the PAHs are believed to be distributed ubiquitously in the ISM [3] [4] and were suggested to be possible carriers of the unidentified infrared bands (UIBs) from  $3.3 - 12.7 \mu\text{m}$  detected in many spectra of nebulae [5]. The PAHs were estimated to hold up to 20% of cosmic carbon based on the modeling of the absorption and emission power in a given radiation field [6]. These PAHs in astrophysical environments were expected to play important roles in the

absorption of UV photons and heat input to the interstellar gas by photo-electric effects [7]. The stability of PAHs against degradation by radiation and high temperature may also have had functional and structural roles in the prebiotic chemistry [8]. Recent studies on the dissociation of PAHs induced by stellar wind particles and UV photon absorption both suggested that the PAHs could be the source of hydrogen molecule in some astrophysical environments [9] [10] [11].

During the past three decades, the PAH hypothesis became widely accepted in astrophysics and initiated numerous theoretical and experimental studies on their physical and chemical properties, the and their interaction with photon and charged particles to clarify their evolution and role in the ISM [12]. Among all the studies, the infrared and electronic spectra are of great interest since they are

directly related to the UIBs and the identification of PAHs in the ISM. The absorption/emission spectra of many PAHs have been extensively investigated from matrix-isolated to gas-phase environments [13] [14] [15] [16] [17] [18].

The interaction with UV photons and cosmic particles are two dominant ways for the PAHs to gain energy in the ISM. Thus the energetic processing of PAHs after the interaction is crucial to determine the size and charge distribution, and the evolution of the PAHs in astrophysical environments. For this purpose, the ionization, dissociation and/or radiative cooling of a large number of PAHs after UV absorption or interaction with charged particles have been studied in detail [19] [20] [21] [22] [23] [24] [25].

Although many works have been done on the PAHs, not even a single PAH species has been identified in the ISM up to now. The complex identification work requires not only the IR signatures but also the photophysics, interaction with cosmic particles or stellar winds particles, as well as possible chemical reactivities of these particular species to build up a clear picture of their role in the ISM [26] [27].

In these contexts, we focus on one of the pyrene smallest PAH: the pyrene molecule ( $C_{16}H_{10}$ ) presented in figure 1 and, in particular, on its ionization cross section when interacting with stellar winds protons in close circum-stellar environment.

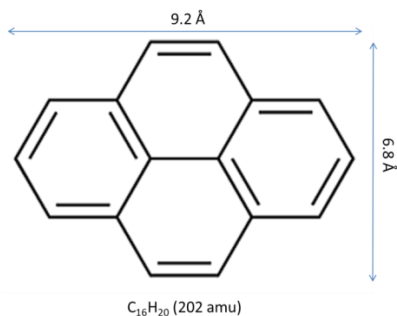


**Figure 1.** Neutral pyrene molecule geometry

A number of studies have been already performed on pyrene molecules including (without been exhaustive) the optical spectra from infrared to UV range [13] [15] [16] and photon-induced dissociation and ionization processes [17] [21]. Up to date the studies on the collision-induced ionization and dissociation processes mainly carried concern the ionization energies, dissociation energies and pathways [28] [24]. No work on the collision-induced ionization cross-section was reported yet. In a recent paper [29], Biswas investigated both experimentally and theoretically differential electron emission cross-section for coronene and fluorene under 3.75 MeV/u  $O^{8+}$  impact. Calculations were carried out with first-order approximation and good agreement with experimental results was obtained. A clear

signature for the plasmon resonance was observed for coronene target.

In this paper, we report on the measurements of the double differential electronic emission cross-section (DDCS)  $\frac{\partial^2 \sigma(E, \theta)}{\partial \omega \partial E}$  of isolated pyrene molecule, induced by protons with velocity of 1.4 to 2.2 atomic units corresponding to 50 to 125 keV.

A similar experimental method had been previously used to study the interaction of DNA/RNA bases with [30] and a detailed description of this method will be given in the coming section. These complete cross-section measurements were compared to the simulations of emitted electrons spectra obtained using a Semi-Classical Trajectory Monte-Carlo approach (SCTMC). The SCTMC method and the comparison with experimental results will be discussed.

## 2. Experimental Set-up

The experimental Set-up presented in figure 2 was developed by the Interactions Ions-material team (IM) of the LCAR laboratory of Toulouse 3 University (UMR 5589).

A continuous ion beam produced in a high-frequency plasma ion source was accelerated to certain kinetic energies: 50, 75, 100 and 125 keV in this experiment series.

The proton beam current obtained after the mass over charge ( $m/q=1$ ) selection through a  $30^\circ$  magnet was around 100 nA. The proton beam was then chopped at 25 kHz frequency by a pair of electrostatic deflectors in front of a 2 mm aperture to produce 500 ns width proton bunches. The temporal structure of the proton beam was used to discriminate signal from the constant background noise.

The obtained collimated proton bunches then entered the collision chamber and intercepted perpendicularly the continuous neutral pyrene molecular jet.

The pyrene molecular jet was obtained by sublimation of pyrene powder in an oven kept at  $70 \pm 2^\circ C$  during the experiments. The pyrene powder was purchased from Sigma-Aldrich with 96% purity and was used without further purification.

The “collision”-induced electrons emitted at  $35 \pm 1^\circ$  from the proton beam axis were analyzed against their kinetic energy through a cylindrical mirror analyzer (CMA) and recorded by a SJUTS (KBL15RS) type channeltron. During the interaction between the incident protons and pyrene molecule, all the particles emitted at  $90^\circ$  with respect to the proton beam direction were collected by a micro-channel plates (MCP) detector associated to a drift tube, as shown in figure 2.

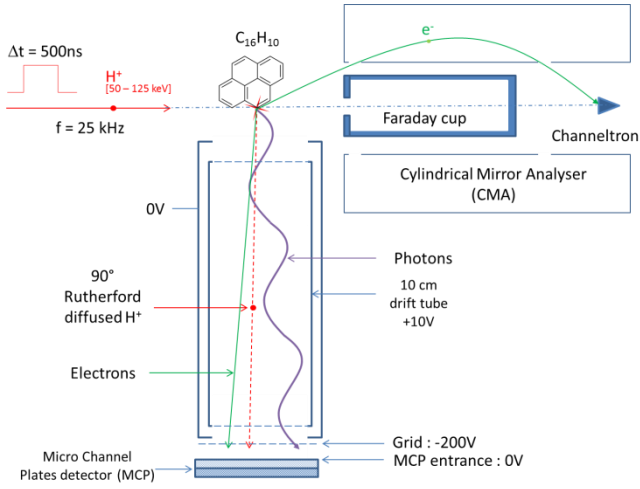


**Figure 2.** Schematic of the experimental setup

Suitable polarizations of the drift tube and MCP (MCP grid at -200 V, drift tube at +10 V) prevent the low energy electrons (< 200eV) and low energy ions to reach the MCP.

The protons scattered at 90° by Rutherford process (at around 90 keV), electrons with energy greater than 200 eV (coming from deep molecular orbitals Auger relaxation processes) and X-UV photons are detected.

The signals on both CMA and MCP detectors were pre-amplified (ORTEC VT120), discriminated (ORTEC 584) and processed by a FastComtek Time-to-digital converter with a resolution of 5 ns.

From the measurements of the MCP various signals and emitted electron recorded by the CMA, absolute measurements of double differential emission cross section (DDCS) at 35° angle are obtained.

### 3. Doubly differential electronic emission cross-section measurements

#### 3.1 Expression of the DDCS and experimental method

Experimentally, the absolute DDCS is linked to the number of electrons ( $N_e$ ) detected by the CMA via the relation:

$$\frac{\partial^2 \sigma_i}{\partial E \partial \Omega_e} = \frac{N_e}{\eta_e \Delta E N_{ip} [\rho L \Omega]_{CMA}} \quad \text{eq. 1}$$

Where  $[\rho L \Omega]_{CMA}$  is a form factor homologous to a surface density. It regroups the absolute density profile of the molecular jet, the length of the interaction region (cross beam intersection of the two crossed beams) and the solid angle seen by the CMA channeltron detector at the emission point.  $\eta_e$  stands for the detection efficiency of the channeltron detector.  $\Delta E$  is the energy bandwidth of the CMA at electron energy  $E$  and  $N_{ip}$  is the number of incoming protons.

Direct measurements of all parameters in eq.1 are experimentally very difficult to achieve with good accuracy and in particular, the absolute density of the molecular jet which appears in the surface density factor  $[\rho L \Omega]$ . To overcome this problem, and get rid of the measurement of the molecular jet density, we have adopted the strategy of simultaneously records: the emitted electrons from pyrene, protons due to Rutherford scattering and particles (electrons and photons) emitted from K-shell ionization of the carbon atoms of the pyrene molecule. Cross sections of these three last processes are well known.

The protons from Rutherford scattering at around 90° from the proton beam axis were counted on the MCP detector, see Figure 2. These scattered protons were induced by low impact parameter collisions on the constituent atoms of the pyrene molecule i.e. mostly carbon atoms. The corresponding total cross-section is analytical and can be easily calculated by summing on the individual Rutherford cross-section of each atom of the molecule (P. Moretto-Capelle, 2006).

$$\frac{\partial \sigma_{\text{totR}}}{\partial \Omega_p} = n_C \frac{\partial \sigma_R(H^+ \rightarrow C)}{\partial \Omega_p} \Big|_{90^\circ} \quad \text{eq. 2}$$

with  $n_C=16$  is the number of carbon atoms in pyrene.

Thus the number of protons scattered at 90° and detected on the MCP ( $N_p^{\text{detected}}$ ) can be written as following according to eq. 2:

$$N_p^{\text{detected}} = \eta_p \frac{\partial \sigma_R}{\partial \Omega_p} [\rho L \Omega]_{MCP} N_{ip} \quad \text{eq. 3}$$

Considering their velocities (2 a.u), the 100 keV incident protons can also easily ionize the K-shell of the carbon atoms in the pyrene molecule. Then 277 eV  $K\alpha_{12}$  X-ray photons as well as electrons produced through the K-shell Auger cascades relaxations effect can be detected by the MCP detector.

According to NIST database, the most abundant primary Auger electrons following Carbon K-shell ionisation are emitted at around 260 eV. Then most of them are not stopped by the 200V polarized grid place in front of the MCP detector (see Figure 2.) and are recorded but others low energy electrons emitted by higher transition of the Auger cascade as well as electrons emitted by Hydrogen are stopped.

The collision induced Carbon- $K\alpha$  Auger emission cross sections are very well documented. H. Paul et al. [31] have found between  $8 \times 10^3$  barn at 35 keV collision energy to  $5.6 \times 10^5$  barn at 200 keV with a maximum of  $10^6$  barn at 500-700 keV.

Moreover, for carbonated molecules such as pyrene, the total Auger emission cross section is directly proportional to the  $n_C$  number of carbon atoms as shown by Biswas et al. [29].

Finally considering that the pyrene molecule was not experimentally oriented, the emitted  $K_\alpha$  photons and Auger electrons are supposed to be emitted isotropically from the pyrene molecule after interaction.

Then, the corresponding differential emission cross-section can be written as the total one (noted  $\sigma_{cK}$ ) divided by the total solid angle  $4\pi$  and multiplied by the number of carbon atoms in pyrene:

$$\frac{\partial \sigma_K}{\partial \Omega_p} = n_C \frac{\sigma_{cK}}{4\pi} \quad \text{eq. 4}$$

The number of X-UV photons and Auger electrons detected on the MCP can be then expressed as:

$$N_{hv}^{detected} = \eta_{hv} \omega_K [\rho L \Omega]_{MCP} N_{ip} \frac{\partial \sigma_K}{\partial \Omega_p} \quad \text{eq. 5}$$

$$N_{Auger}^{detected} = \eta_{eA} (1 - \omega_K) [\rho L \Omega]_{MCP} N_{ip} \frac{\partial \sigma_K}{\partial \Omega_p} \quad \text{eq. 6}$$

Where  $N_{hv}^{detected}$  is the number of  $K_\alpha$  X-ray photons detected by the MCP,  $N_{Auger}^{detected}$  detected is the number of detected Auger electrons,  $\eta_{hv}$  is the MCP efficiency for X-UV photons at 277 eV and  $\eta_{eA}$  the MCP efficiency for 260 eV electrons.

The  $\omega_K$  factor is corresponding to the carbon fluorescence yield, which is very low for the photon emission following K-shell ionization :  $\omega_K = 0.0035 \pm 10\%$  [32]. Even if the main process of relaxation is therefore the Auger effect (i.e.  $N_{Auger}^{detected} > N_{hv}^{detected}$ ), both processes were taken into account for the experimental DDCS estimation.

The particles from processes mentioned above (Rutherford scattered protons, Carbon  $K_\alpha$  X-ray emission and Auger electrons) are detected by the MCP detector without any possible differentiation and the total number of counts detected by the MCP can be written as:

$$N_{MCP} = N_p^{detected} + N_{hv}^{detected} + N_{Auger}^{detected} \quad \text{eq. 7}$$

$$N_{MCP} = N_{ip} [\rho L \Omega]_{MCP} \left( \eta_p \frac{\partial \sigma_R}{\partial \Omega_p} + \eta_{eA} \frac{\partial \sigma_K}{\partial \Omega_p} \left( \left( \frac{\eta_{hv}}{\eta_{eA}} - 1 \right) \omega_K + 1 \right) \right) \quad \text{eq. 8}$$

From the ratio between the number of recorded electrons ( $N_e$ ) on the channeltron (eq. 1) and the number of particles ( $N_{MCP}$ ) detected on the MCP detector (eq. 8), we can then express the pyrene molecule's electronic emission DDCS as:

$$\frac{\partial^2 \sigma_i}{\partial E \partial \Omega_e} = \frac{N_e}{N_{MCP}} \frac{\Gamma}{\eta_e \Delta E} \left( \eta_p \frac{\partial \sigma_R}{\partial \Omega_p} + \eta_{eA} \frac{\partial \sigma_K}{\partial \Omega_p} \left( \left( \frac{\eta_{hv}}{\eta_{eA}} - 1 \right) \omega_K + 1 \right) \right) \quad \text{eq. 9}$$

Where  $\Gamma = \frac{[\rho L \Omega]_{MCP}}{[\rho L \Omega]_{CMA}}$  only depends on the relative density profiles and the characteristics of the detectors in terms of solid angle seen by each detector, but no more depends on the absolute density of the pyrene molecular jet. Moreover, this DDCS formulation doesn't depend on the number of incident protons, which avoids precise measurement of the proton beam intensity.

In this series of experiment, the proton energy range was 50 to 125 keV with 25 keV step. For such energies, the  $90^\circ$  Rutherford scattering cross-section is small comparing to the inner shell ionization cross-section. Thus, the main relaxation process will be the Auger electron emission and a coarse approximation of the DDCS can be expressed as:

$$\frac{\partial^2 \sigma_i}{\partial E \partial \Omega_e} \sim \frac{N_e}{N_{MCP}} \frac{\Gamma}{\Delta E} \frac{\eta_{eA}}{\eta_e} \frac{\partial \sigma_K}{\partial \Omega_p} \quad \text{eq. 10}$$

Experimental determination of each parameter in eq. 10 will be described in the next paragraphs.

### 3.2 Experimental Evaluation of the $\Gamma$ factor

The evaluation of the  $\Gamma$  term requires the relative density profile of the gas-phase pyrene molecule jet. The relative density profile was estimated by measuring the deposit thickness profile on a glass surface which had been hold perpendicularly towards the molecule jet direction in the collision region with a deposit time of two hours under the same experimental conditions (oven temperature  $70^\circ \text{C}$  and pressure  $10^{-7}$  Torr). Then the glass piece was scanned by a densitometer and a deposit thickness profile was obtained, as shown in figure 3.

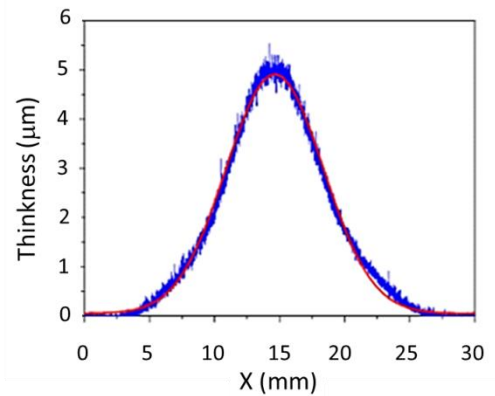


Figure 3. Schematic of the experimental setup

The  $\Gamma = \frac{[\rho L \Omega]_{MCP}}{[\rho L \Omega]_{CMA}}$  term was then estimated by Monte-Carlo simulation [30] which included the relative density profile measured above, the size of the projectile beam (2 mm diameter) and the geometrical characteristics i.e the relative positions, angles of detection, opening angle etc of the MCP and CMA spectrometers.

To achieve the simulation,  $10^6$  initials conditions have been randomly generated (positions according to intersection between beam and molecular beam profile as well as isotropic random direction for the velocity vectors). The  $\Gamma$  factor was then deduced from the ratio of the number of particles arriving on the MCP and the number of particles passing through the exit slit of CMA, we found :

$$\Gamma = 0.92 \pm 0.02$$

### 3.3 Measurement of the MCP yield $\eta_p$ for 90° Rutherford scattered Protons

The MCPs used in these experiments are F4293-07 module manufactured by Hamamatsu. In order to measure the MCP yield  $\eta_p$  for Rutherford scattered protons, the MCP detector was mounted on a retractable manipulator in front of a Faraday cup and directly exposed to the incident proton beam. The proton beam energies were chosen from 40 to 105 keV which corresponds to the final kinetic energies of the 90° Rutherford scattered protons with initial kinetic energies from 50 to 125 keV. Two methods have been used for the absolute MCP yield measurement : one using a pulsed proton beam and the second using a continuous beam.

In the first method, the pulsed beam allows us to control the number  $N$  of ions per pulse, the probability to detect at least one ion at each pulse is then given by:

$$P = 1 - (1 - \eta_p)^N \quad \text{eq. 11}$$

One has to achieve  $N < 1$  in order to have  $P \sim \eta_p$ . To obtain this, a continuous beam of intensity  $I_0 = 100$  pA pulsed with width  $\delta t = 1$  ns gives average number  $N \sim 0.6$  per pulse.

Then the MCP detection efficiency can be express as :

$$\eta_p = \frac{N_c e}{\nu I_0 \delta t} \quad \text{eq. 12}$$

where  $N_c$  is the count rate (in  $s^{-1}$ ) on the MCP and  $\nu = 30$  kHz stands for the pulse frequency ( $e$  is the electronic charge). The MCP detection efficiency was measured to be constant over 30 – 75 keV range and close to unity:

$$\eta_p = 1 \pm 0.05$$

In the second method, the MCP detector was exposed directly to a weak and stable continuous proton beam of intensity  $I_0 = 20$  fA, monitored by a Faraday cup and a Sub-Ampere multimeter (Keythley). The detection efficiency is then simply given by :

$$\eta_p = \frac{N_e}{I_0 T} \quad \text{eq. 13}$$

where  $N$  is the number of detected protons during the acquisition time  $T$  and  $I_0$  the intensity of the weak beam. With this direct method we obtained  $\eta_p = 1.01 \pm 0.05$  in good agreement with the first method.

Such high detection efficiency near to unity is a consequence to the high kinetic energy of the protons which create secondary electrons on the MCP efficiently as well as the present a repeller grid (negative potential) placed in front of the MCP detector (B. Deconihout, 1996).

### 3.4 MCP yield $\eta_{eA}$ for Carbon $K_\alpha$ photons

As mentioned before, we assumed that only UV photons from the ionization of the  $1s^2$  subshell of the carbon atoms can be detected on the MCP, the corresponding photon energy is 277 eV. The detection efficiency was extracted from the data for carbon  $K_\alpha$  line efficiency given by Hamamatsu: a value  $\eta_{eA} = 0.28 \pm 0.08$  was retained. The contribution of photons to the detected signal on the MCP is relatively small so a precise measurement of this efficiency is not critical for the absolute cross section measurement.

### 3.5 Channeltron yield $\eta_e$ of the CMA

In order to calibrate the efficiency of the channeltron detector used inside the CMA electron spectrometer, a specific experimental setup was designed. Its principle is similar to that described by [33] and its schematics and CAO are illustrated in figure 4.

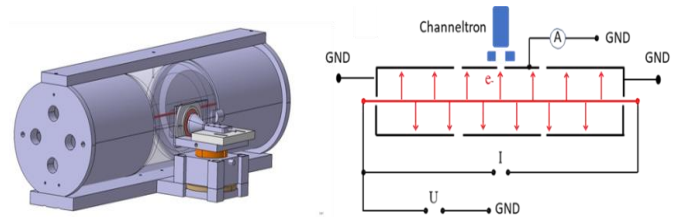


**Figure 4.** Experimental set-up for channeltron efficiency measurement

This experimental setup consists of three spaced cylinders. The two external cylinders are 10 cm long and the middle one is 7 cm diameter. The middle cylinder was isolated from the two neighboring grounded cylinders and had a hole of 1 mm diameter on its sidewall.

A tungsten wire going through the center of the three tubes was heated up by a  $\sim 1$ A DC current and floated to an adjustable negative potential  $U$  [0 - 1000V]. Thus, inside the central cylinder, the thermal electrons emitted from the wire (cathode) penetrating into a uniform radial electric field and acquired well-defined kinetic energy with respect to the applied potential between the wire and the surface of the central tube. Electrons going through the hole on the central cylinder were counted by the channeltron mounted behind the hole (with the same montage as in the CMA). To stop the secondary electrons possibly produced on the inner wall of the hole, a polarized annular electrode was installed between the hole and the channeltron detector to allow only direct electrons to pass.

The middle cylinder was connected to a sub pico-ammeter (module 617 from Keithley) to measure the electronic current  $I_{\text{cylinder}}$  collected over its entire lateral surface. The surface ratio between the lateral surface and the hole was  $\delta = 2.4 \times 10^4$ . Thus the corresponding current through the hole can be calibrated as:

$$I_{\text{hole}} = \frac{I_{\text{cylinder}}}{\delta} \quad \text{eq. 14}$$

By comparing the count rate of the channeltron detector and the calibrated current  $I_{\text{hole}}$ , detection efficiencies versus different incident electron kinetic energies were obtained.

The measured detection efficiencies was varying from  $\eta_e = 0.62 \pm 0.02$  to  $\eta_e = 0.75 \pm 0.05$  for incident electron energy from 100 eV to 1 keV respectively. An average efficiency of  $0.7 \pm 0.1$  was retained for the cross section measurements.

The electron transmission inside the CMA spectrometer was also evaluated. For 25 eV electrons the total scattering cross-section is about  $1.2 \times 10^{-15} \text{ cm}^2$  for  $\text{N}_2$  molecule [34] and about  $1.8 \times 10^{-15} \text{ cm}^2$  for  $\text{H}_2\text{O}$  molecule [35]. The gas density under our experimental conditions ( $P \sim 10^{-8}$  Torr) was about  $10^9 \text{ cm}^{-3}$ , therefore the mean free path was estimated to be about 8 km far longer than the trajectory length inside the CMA spectrometer (around 20 cm). We can then reasonably assume that the spectrometer transmission is 100% for measured electrons.

### 3.5 Noise reduction and $N_e^{\text{detected}}$ , $N_{\text{MCP}}^{\text{detected}}$ Measurements

In order to discriminate the  $N_e^{\text{detected}}$  and  $N_{\text{MCP}}^{\text{detected}}$  counts against the noise counts, a pulsed proton beam was used, so that the real signals were correlated temporally to the proton bunches. An example of raw histogram for 100 keV incident protons and 50 eV electrons detected on the CMA (36 h acquisition) is presented in figure 5.

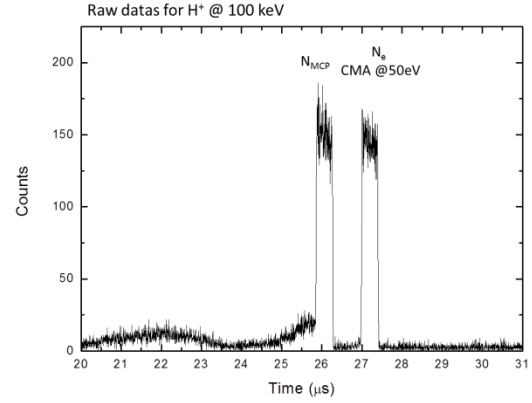


**Figure 5.** Exemple of Raw Data histogram detected on the MCP and the CMA.

The temporal width of both peaks (counts on MCP and on CMA) was 500 ns corresponding to the temporal width of the incident proton bunches. If long enough to get sufficient statistic, such a temporal width was large comparing to the MCP arrival time differences between the Rutherford scattered protons, emitted Auger electrons and the X-UV photons coming from pyrene molecule, thus these three processes can't be temporally discriminated. The measured  $N_{\text{MCP}}$  is then the one mentioned in eq. 7 and 8.

The long time scale background signal covering tens of microsecond corresponds to the asynchronous low velocity ions from the fragmentation of pyrene molecule. This cationic background signal was removed to evaluate  $N_{\text{MCP}}$ .

The residual continuous background on the MCP coming from external noise is around 1 to 5 counts per channel over an integrating time of several days and can be then neglected.

## 4. SCTMC simulation methods for total and DDCCS calculations

Classical Trajectory Monte-Carlo (CTMC) has been early [36] and intensively used and succeeded in the treatment of ion-atom collision [37] [38] and ion/molecule collision [39] [30]. In order to estimate the total and double differential electronic emission cross-sections of pyrene molecule as well as to compare with our experimental results, we have developed a fast optimized 3D Semi-Classical Trajectory Monte Carlo code. In these simulations, classical electrons and proton trajectories in the molecular potential derived from quantum calculations are performed. Typical keV proton-pyrene interaction and pyrene electronic emission (ionization) occurs at very short time scale (fs) comparing to nuclear motion, thus the pyrene molecule nuclei motions were not considered.

The numerical method implemented to integrate differential equations was a basic adaptive Runge Kutta method at the 4th-5th order (RKF45) with auto-adaptive

relative step precision fixed from  $10^{-5}$  to  $10^{-8}$  to ensure satisfying total energy conservation over the calculated trajectory [40] and to achieve a reasonable calculation time per trajectory. Random numbers generation was done using Mersenne twister MT19937 algorithm [41].

#### 4.1 SCTMC Initial Pyrene electron position and velocity

The initial position of the electron was randomly drawn following the distribution of the probability of presence deduced from the square of molecular orbitals (MO) wave function of pyrene molecule. The norm of the initial velocity of the electron was obtained through energy conservation knowing both binding energy of the MO and molecular potential  $V_m$ . The direction of the initial velocity is chosen randomly. Geometry of the MO, binding energy and  $V_m$  have been calculated using Gamess code [42] using 6-31G(d,p) basis set at the Self Consistent Field (SCF) level of theory in D<sub>2h</sub> symmetry. An example of initial position distribution obtained for 50 103 electrons randomly picked up in the pyrene HOMO orbital is shown in figure 6:

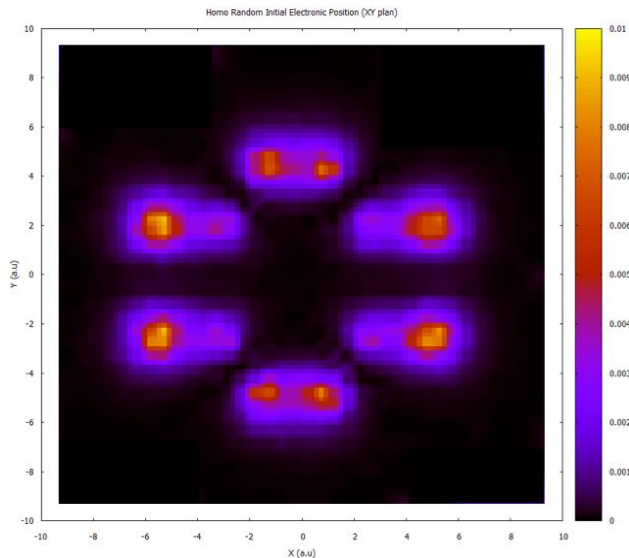


**Figure 6.** Example of HOMO random initial positions of the electron of pyrene molecule.

Due to the consideration of the computing time, only HOMO-x, with  $x=0, 1, 3, 5, 10, 15$  and  $36$  are considered.

#### 4.2 SCTMC Initial proton position, molecular orientation and reference surface

The molecular orientation was chosen randomly with uniform angle distribution, reproducing the experimental conditions.

The proton initial position was selected randomly in a reference surface  $S_{ref}$  [30] perpendicular to the velocity vector of the incoming protons as shown in figure 7, at a distance of ten times the molecular radius (pyrene classical

radius  $R_{mol}= 8.64627$  a.u.) where the molecular potential and electron-proton force field is close to zero.

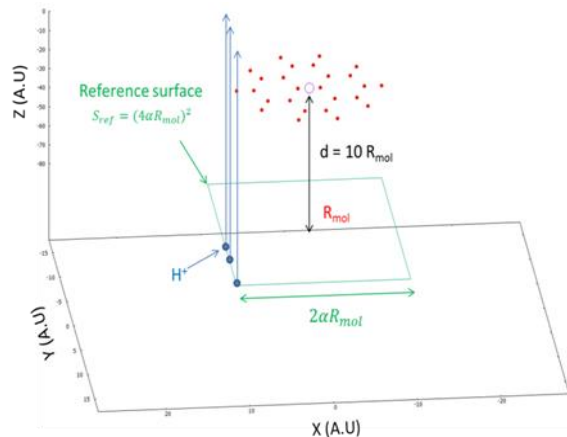


**Figure 7.** Simulation geometries and reference surface definition (in atomic units).

The  $S_{ref}$  is then:

$$S_{ref} = 4\alpha^2(R_{mol}) \quad \text{eq. 15}$$

This reference surface was “empirically” chosen in a way that protons initially starting at the edge of this surface didn’t induce any ionization of the molecule no matter where the initial position of the electron in the molecule was or what the molecular orientation was. The factor  $\alpha$  was adjusted by iterative simulations increasing its value from 1 till no ionization event is detected for edge protons. In present CTMC simulations we found  $\alpha=1.45$ .

The corresponding reference surface is then:  $628.714 \text{ a.u.}^2$  ( $176.058 \cdot 10^{-16} \text{ cm}^2$ ). For this surface, 15 million trajectories with proton starting from its edge were performed showing no ionization event.

Then, the molecular orbital cross section can be writing as a function of  $S_{ref}$  and ionization probability as:

$$\sigma_{Mo} = \frac{N_k}{N_{traj}} \cdot S_{ref} \quad \text{eq. 16}$$

Where  $N_{traj}$  is the total number of generated trajectories and  $N_k$  is the number of trajectories conducting to the event of interest. The ionization process under interest will be characterized by the emission of the electron in the continuum of the molecule at an energy  $E$  and a  $\theta$  angle relatively to the proton velocity vector.

#### 4.3 SCTMC Potential

For these simulations, the interacting potential are the coulombic interaction between electron and proton  $V_C^{p,e^-}$  and the molecular potential  $V_m$  of the singly ionized pyrene molecule in its fixed neutral geometry. Individual atomic

motions or molecular recoil are not taken into account seen ionization occurs in very short time scale (fs) compare to any atomic motions (ps).

For numerical convenience, the molecular potential  $V_m$  was approximated by a sum over each atom of the molecule of a screened potential function and can be written as:

$$V_m(\vec{r}) = \sum_{i=0}^n Z_i \frac{e^{-k_i|\vec{r}-\vec{R}_i|}}{|\vec{r}-\vec{R}_i|} \quad \text{eq. 17}$$

Where  $r$  and  $R_i$  are the position of electron and atom  $i$ . The screen function coefficient ( $k_i$ ) and the effective atomic charge ( $Z_i$ ) were adjusted to reproduce the molecular potential obtained with the Gamess code.  $Z_i$  was found to be equal to 4 and 1 and  $k_i=1.55 \text{ a.u}^{-1}$  and  $1.45 \text{ a.u}^{-1}$  for carbon and hydrogen atoms respectively.

Figure 8 presents an example of electron classical trajectory starting from HOMO orbital in the fitted  $V_m$  molecular potential without  $e^-$ /proton interaction.

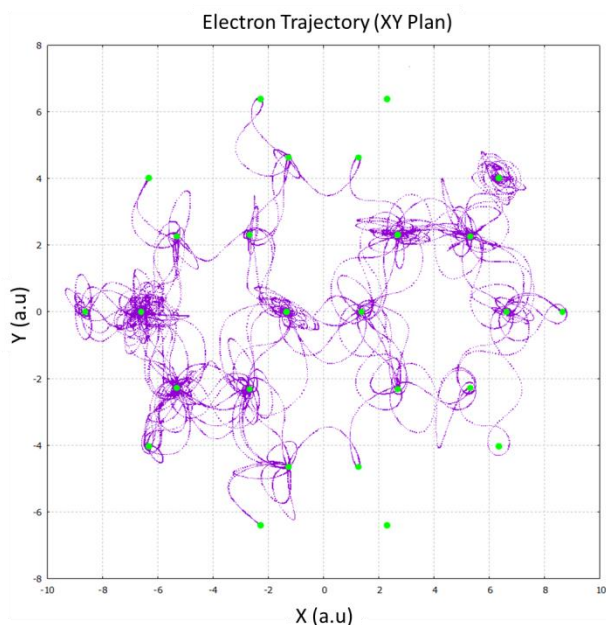


**Figure 8.** Classical trajectory, projected in the plane of the molecule, of an electron of the HOMO in the analytical molecular potential  $V_m$ . The green dots represent the positions of the atoms of the Pyrene molecule.

The figure 8 shows a very good stability of the electron classical motion in the fitted molecular potential for a long integration time scale (typically  $>100 \text{ ps}$ ). Possible numerical "accidental" ionization linked, for example, to the discontinuity of the fitted potential near each atom and/or to the minimum pitch/precision couple set for the RKF45 method have been tested using energy conservation criteria (with respect to the virial theorem). Compromise between precision, stability and total duration of each trajectory was

performed. A transient variation of less than 1% of the total initial energy was tolerated.

For the MO considered, the number of detected "accidental" ionization in the  $V_m$  potential (without proton interaction) were much lower than 1/1000 simulated trajectories. The ionization occurred essentially at very long integration time (10th of ps) comparing to the typical interaction time between the electron and the proton (At a 2 a.u velocity, the protons travels hundred times the pyrene molecular radius in  $\sim 20 \text{ fs}$ ).

#### 4.4 CTMC: Simulated Cross Sections

For each MO, the partial ionization cross-section was evaluated over more than 10 million trajectories with typical simulations running over 100 random molecular orientations, 200 initial electron positions and 500 initial proton positions.

This large number of trajectories per orbital was sufficient to ensure full convergence of the total cross-section and to guaranty enough angular statistics for DDSCS calculation. The more bounded is the M.O. (electronic densities close to molecular atoms) the more trajectories simulations takes time (2 Weeks /orbitals) mostly due to the auto-adaptive stepper of the used numerical method. Then for Homo-36 "only" 2 million trajectories were evaluated and K-shell M.O. ionization cross-sections were not calculated. Missing orbitals partial ionization cross-sections will be interpolated (see paragraph 5).

We assume in our simulation that ionization of the electron was achieved when its distance from the molecule became greater than 1.5 time the molecular radius before proton reaches 10 time the molecular radius. The convergence of the electron kinetic energy was also checked as well as possible to determine if we observe a real ionization or a capture on the proton.

Trajectories of ionized electrons and outgoing proton were then extended (without molecular potential interaction i.e. only electron-proton interaction) at a long distance from the molecule ( $1000 \times R_{mol}$ ) to guaranty a good proton/electron emission angle convergence. Final angles  $\theta$  (referenced by the incoming proton axis), asymptotic velocities vectors and kinetic energy  $E$  of the ionized electrons were recorded.

The total ionization cross-section were derived from the eq. 14 for each MO including the MO multiplicity (close-shell i.e. 2 electrons per MO), so the total cross-section can be written as:

$$\sigma_{total} = 2 \sum_{MO} \sigma_{MO} \quad \text{eq. 18}$$

Similarly, the double differential cross-section was obtained from the  $N_{MO}(E, \theta)$  electron energy, angle 2D histogram with  $\delta E$  and  $\delta \theta$  the binning resolution such as:

$$\frac{d\sigma_{tot}}{dE d\Omega} = 2 \sum_{MO} \frac{N_{MO}(E, \theta)}{2\pi \sin(\theta) \delta E \delta \theta} \frac{S_{ref}}{N_{traj}} \quad \text{eq. 19}$$

For these simulations including the proton/electron interaction, the number of “false” ionization were higher than in the case of single electron/molecular potential interaction discussed in paragraph 4.3, especially for core-MO as shown in table 1 which presents the total number N of simulated trajectories per MO and number of rejected trajectories N\*.

**Table 1.** Number of rejected trajectories per MO

M.O	N	N*	N*/N
Homo	$10^7$	714354	7,14%
Homo-1	$10^7$	749764	7,49%
Homo-2	$10^7$	839546	8,39%
Homo-5	$10^7$	1197211	11,97%
Homo-10	$10^7$	1272417	12,72%
Homo-15	$10^7$	1363274	13,63%
Homo-36	$2.10^6$	676775	33,83%

This high number of bad trajectories for deeper shell orbitals is related to the less relevant sampling/interpolation of the wave function for core-MO. Indeed, the grid step covering the molecular volume extracted from the Gamess orbital calculation was not adaptive. Consequently, the regions with a high density of probability of presence or those having a strong gradient (which was the case for core-MO) may not be well sampled when determining the initial classical position of the electron. Then the electrons being potentially drawn at the same "places" can create redundancies in the initial conditions and the trajectories even for “good” trajectories (i.e. those respecting the 1% energetically criteria mentioned above (see 4.2)). This will result in an overestimation of the MO ionization cross-section of the core-MO, and a “fictive” increase of the convergence speed (in term of the number of simulated trajectories) of the total CTMC ionization cross-section simulations. This over-sampling of the core-MO may also induce a lower dispersion around the converged cross-section value which consequently conducted artificially to a drastic underestimation of the associated statistical uncertainty.

The CMTC cross-sections were finally calculated by removing the wrong trajectories. However, in order to include these numerical biases we have chosen to take into account bad trajectories for cross-section uncertainties estimation.

## 5. Results and discussions

### 5.1 Total ionization cross-section

For each considered MO, the figure 9 presents the corresponding partial ionization cross-section as a function of the number of trajectories calculated, for 100keV/pyrene interaction.

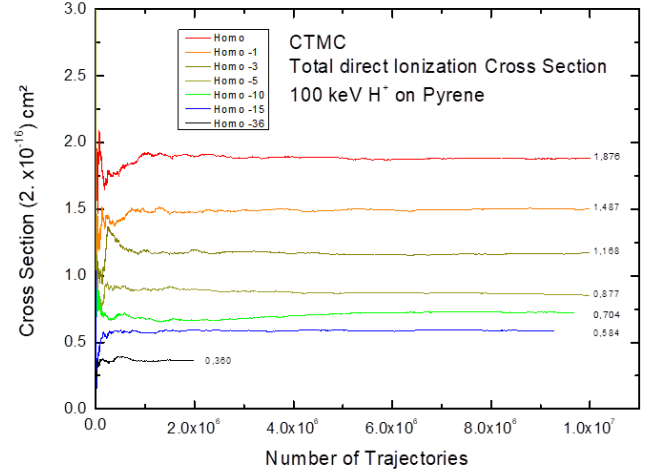


**Figure 9.** Convergence of the MO total ionization cross-section as a function of the number of trajectories.

As we can see from Figure 9, the partial cross-section were well converged for every calculated orbitals after 8 Millions of trajectories. Then from the calculated HOMO-x, SCTMC cross-section simulation, intermediate HOMO orbitals ionization cross-sections were extrapolated.

Phenomenologically the total cross-section seems to follow a continuous exponential decay with the MO energies as shown in figure 10.

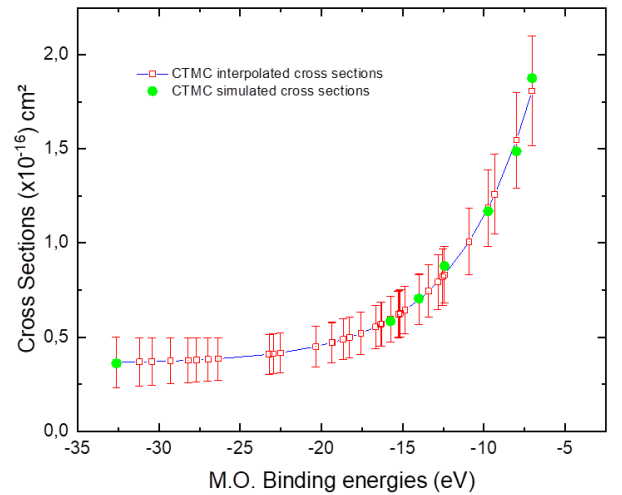


**Figure 10.** MO SCMTC cross-sections (green dots), interpolated MO cross-sections from SCTMC cross-section (red squares).

The total uncertainty estimation takes into account statistical dispersion (95% of confidence) around the converged values evaluated over the last 1 Million trajectories, the uncertainty relative to the “bad” trajectories and the uncertainty of the exponential fitting curve.

Finally, summing over all MO partial cross section according to eq. 18, the total SCTMC single ionization cross-section of pyrene at 100 keV collision energy was estimated to:

$$\sigma_{\text{SCTMC}} = (47.59 \pm 10.03) \times 10^{-16} \text{ cm}^2$$

This value is in good agreement with the geometrical cross-section:  $49.7 \times 10^{-16} \text{ cm}^2$ .

In order to check once more this value, we have used Rudd’s electron emission cross-section for 100 keV proton impact on molecules. Rudd et al obtained a cross-section of  $7.4 \times 10^{-16} \text{ cm}^2$  and  $2.26 \times 10^{-16} \text{ cm}^2$  for  $\text{CH}_4$  and  $\text{H}_2$  respectively [43]. From those cross-sections and assuming that additivity rules apply, we can write  $\sigma(\text{C}_{16}\text{H}_{10}) = 16\sigma(\text{C}) + 10\sigma(\text{H})$  with  $\sigma(\text{C}) = \sigma(\text{CH}_4) - 2\sigma(\text{H}_2)$  and  $\sigma(\text{H}) = \sigma(\text{H}_2)/2$ , a total cross-section of  $57.4 \times 10^{-16} \text{ cm}^2$  was then obtained also in good agreement with the CTMC calculated one.

It must be noted that photoionization cross-section for pyrene or coronene is about 32 Mb per carbon [44] i.e.  $51.2 \times 10^{-16} \text{ cm}^2$  for the pyrene molecule which is comparable to the total ionization cross-section by 100 keV proton found in this work. So the ionization via solar wind particles is as effective as UV photons (for comparable flux) in close circumstellar environment.

## 5.2 Results on Doubly Differential Cross Sections

From SCTMC trajectories the partial double differential ionization cross-sections for each considered molecular orbital and for 100 keV incident proton was evaluated using eq. 15.

To build the required  $N_{\text{MO}}(E, \theta)$  2D histogram, steps of  $\delta\theta = 10^\circ$  and  $\delta E = 0.1 \text{ a.u.}$  were used. Example of obtained results for Homo and Homo-36 orbitals are presented in figure 11.

The obtained partial DDCS peaked at low electrons energy and essentially in the forward direction ( $\theta$  from  $0^\circ$  to  $20^\circ$ ) due to Post Collision Interaction (PCI) effect. One manifestation of this PCI effect is the Electron Capture in the Continuum (ECC) [45] corresponding to the peaks in figure 11 and obtained for all molecular orbitals at  $\theta \sim 0^\circ$  and kinetic energy  $E \sim 2 \text{ a.u.}$  i.e. electron having the same velocity and direction as the 100 keV proton projectile but not bounded to it.

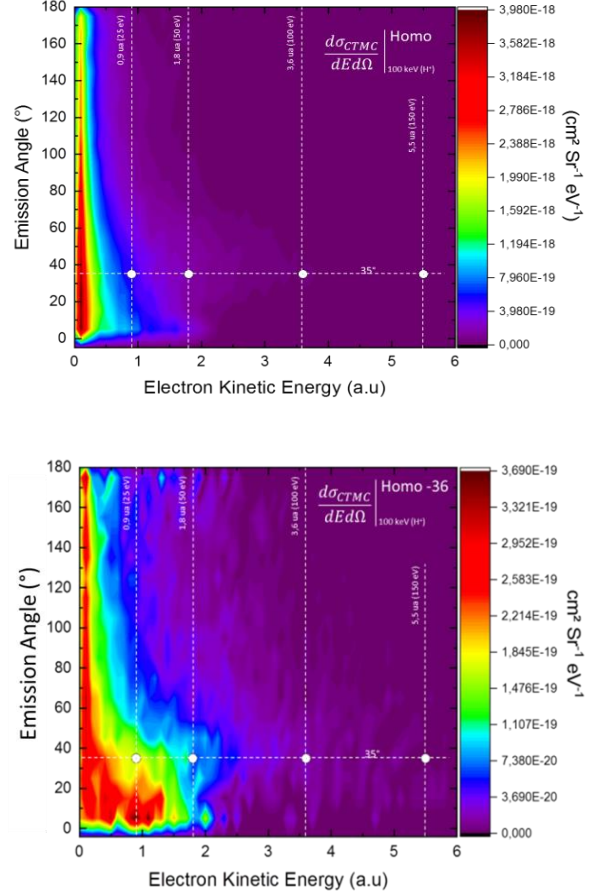


**Figure 11.** DDCS of pyrene electron emission for HOMO (upper part) and HOMO-36 (lower part) MO interacting with 100 keV protons. White dots correspond to the experimental conditions ( $35^\circ$ , 25 – 125 keV protons).

In the SCTMC calculation, it was found that the electron energy distribution extended to higher energy when the electron emission came from more internal valence orbitals. The inner MO corresponds to higher binding energy and ionization potential and leads to higher energy in the energy distribution, this is qualitatively consistent with the empirical Rudd’s formula (for single differential cross section, nevertheless) [46]:

$$\frac{d\sigma_{\text{tot}}}{dE} = 5\pi a_0^2 \alpha^3 I_H^2 \sum_i \frac{N_i}{I_i^3} \frac{(T/I_i)^{\beta-1/2}}{4+(T/I_i)^{2\beta}} e^{-\frac{\alpha E}{\sqrt{I_i T}}} \quad \text{eq. 20}$$

Where  $\alpha$  and  $\beta$  are adjustable constants depending on target,  $I_i$  and  $N_i$  binding energy and occupation of level  $i$ ,  $E$  the kinetic energy of the emitted electrons and  $T$  the energy of electron with the same velocity as the projectile. Experimental total electronic emission DDCS were measured at  $\theta = 35^\circ$  for 25, 50, 100 and 150 eV, the corresponding partial SCTMC DDCS were extracted ( $\theta = 35 \pm 5^\circ$ ,  $E = E_0 \pm 0.05 \text{ eV}$ ). As for the case of partial MO ionization cross-

section, non-calculated partial DDCS can be estimated by interpolation as show in figure 12.

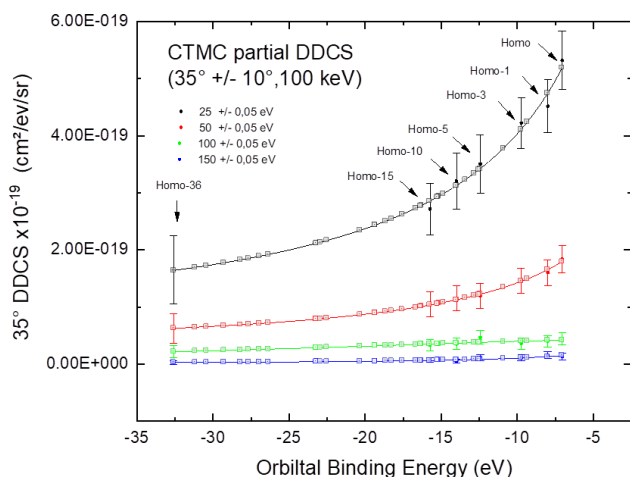


**Figure 12.** partial SCTMC DDCS interpolation for pyrene electron emission from HOMO-x (x=0 to 36) and various electron emission energies : 25, 50, 100 and 150 eV

The total SCTMC DDCS were then evaluated by summing each partial DDCS over all the molecular orbitals taking into account their occupancy.

**Table 2.** Total DDCS from CMTC calculations for 100 keV protons and experimental DDCS at 35°

Ek	$d\sigma(35^\circ, E_k)/dE d\Omega$ (cm <sup>2</sup> sr <sup>-1</sup> eV <sup>-1</sup> ) x10 <sup>-19</sup>				
	50 keV Exp.(err)	75 keV Exp.(err)	100 keV CTMC(err)	100 keV Exp.(err)	125 keV Exp.(err)
25 eV	4.26 ±1.70	20.23 ±8.09	100.7 ±21.5	43.81 ±17.53	51.85 ±20.74
50 eV	1.04 ±4.16	5.51 ±2.21	36.5 ±7.8	11.37 ±4.55	14.86 ±5.94
100 eV	0.08 ±0.04	0.78 ±0.32	11.9 ±2.6	2.16 ±0.87	3.08 ±1.24
150 eV	0.007 ±0.003	0.12 ±0.05	2.82 ±0.59	0.49 ±1.98	0.86 ±0.35

Experimental DDCS measured at 35° for 50, 75, 100 and 125 keV protons and simulated (35°, 100 keV proton) CTMC DDCS have been regrouped in table 2 and are presented in figure 13 as a function of emitted electron energies.

A reasonable agreement was obtained between CTMC simulations and the experimental DDCS at 100 keV collision energy even if the CTMC DDCS was always overestimated comparing to the measured one with a factor of 2.3 at low electron energy and a factor of 5.75 at 150 eV.

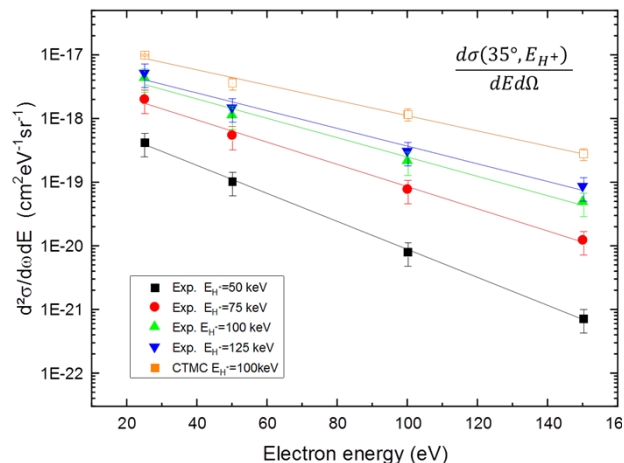


**Figure 13.** Comparison of the DDCS between experiment and CTMC calculations

This overestimation of the DDCS cannot be attributed to numerical problems or limited statistics since total cross-section was well converged and that CTMC overestimated uncertainties doesn't allow any overlap with experimental datas. But the Semi Classical model is as expected a coarse approach that gives only an order of magnitude of the DDCS.

Both experimentally measured and CTMC simulated DDCS in figure 13 highlights a strong population of low energy electrons which seems to be a general phenomenon in ion-atom collision [47] or ion/molecule [48].

A strong increase of the cross-section with collision energy was experimentally observed from 50 to 125 keV and the maximum cross-section was reached at around 100-125 keV according to the quasi equivalent DDCS in this energy range. The DDCS obtained at 50 keV was quite low and might be underestimated. The experimental DDCS at 35° decrease almost exponentially with the energy of emitted electrons.

## 6. Conclusion

We have investigated the electron emission of a PAH molecule, the pyrene, submitted to solar wind particles, namely keV protons, both experimentally and theoretically through the Semi-Classical Trajectory Monte-Carlo method.

Absolute differential cross-sections were for the first time obtained and a reasonable agreement between experiment and semi-classical CTMC calculation achieve. The total cross-section of ionization process obtained from the CTMC method was comparable with the geometrical cross-section of the pyrene molecule.

The measurement of absolute quantities of such cross-section are important in astrophysics, has the reaction yields of such ion/molecule collision process are directly related to the cross-section. With the knowledge of the cross-section, the fragmentation patterns of the molecule can be quantified

in an absolute way so that even the secondary molecular species generated by ionization process can be quantified. The ionization cross-sections obtained in the current work are comparable to the Photoionization cross-section. Therefore, such collision processes have to be taken into account for the PAHs physico-chemistry in Circumstellar environment especially in compact planetary nebulae.

### Acknowledgements

We thank's the Labex Next (<http://www.next-toulouse.fr/>) for its financial support to these researches.

### References

- [1] O. V. S. a. R. K. J. Sudip K Samanta, «Polycyclic aromatic hydrocarbons: environmental pollution and bioremediation,» *Trends in Biotechnology*, 20(6);, pp. 243-248, 2002.
- [2] H. Yu, «Environmental carcinogenic polycyclic aromatic hydrocarbons: photochemistry and phototoxicity,» *Journal of environmental science and health. Part C, Environmental carcinogenesis & ecotoxicology reviews*, 20(2), 2002.
- [3] A. L. a. J. L. Puget, «Identification of the 'unidentified' IR emission features of interstellar dust?,» *Astronomy and Astrophysics*, 137, pp. 5-8, 1984.
- [4] A. G. G. M. T. a. J. R. B. L. J. Allamandola, «Polycyclic aromatic hydrocarbons and the unidentified infrared emission bands - Auto exhaust along the Milky Way,» *The Astrophysical Journal Letters*, 290, pp. 25-28, 1985.
- [5] A. L. a. L. D'Hendecourt, «Are polycyclic aromatic hydrocarbons the carriers of the diffuse interstellar bands in the visible?,» *Astronomy and Astrophysics*, 146, pp. 81-85, 1985.
- [6] A. L. a. P. M. C. Joblin, «Contribution of polycyclic aromatic hydrocarbon molecules to the interstellar extinction curve,» *The Astrophysical Journal Letters*, 393, pp. 79-82, 1992.
- [7] E. L. O. B. a. A. G. G. M. Tielens, «The photoelectric heating mechanism for very small graphitic grains and polycyclic aromatic hydrocarbons,» *The Astrophysical Journal*, 427, pp. 822-838, 1994.
- [8] D. W. D. A. K. a. P. E. Joost Groen, «Polycyclic Aromatic Hydrocarbons as Plausible Prebiotic Membrane Components,» *Origins of Life and Evolution of Biospheres*, 42(4), pp. 295-306, 2012.
- [9] P. M.-C. P. C. C. D. M. S. a. R. C. J.-P. Champeaux, «Is the dissociation of coronene in stellar winds a source of molecular hydrogen? application to the HD 44179 nebula,» *Monthly Notices of the Royal Astronomical Society*, 441(2):1479–1487, June 2014, pp. 1479-1487, 2014.
- [10] J. S. a. N. C. P. Yi Fu, «Photon-induced Formation of Molecular Hydrogen from a Neutral Polycyclic Aromatic Hydrocarbon: 9,10-dihydroanthracene,» *The Astrophysical Journal*, 744(1), p. 61, 2012.
- [11] S. C. M. S. R. H. a. T. S. L. Boschman, «H<sub>2</sub> formation on PAHs in photodissociation regions: a high-temperature pathway to molecular hydrogen,» *Astronomy Astrophysics*, 579, 2015.
- [12] C. J. a. A. G. G. M. Tielens, «PAHs and the universe: a symposium to celebrate the 25th anniversary of the PAH hypothesis, volume 46. EAS, EDP Sciences,» 2011.
- [13] P. B. A. L. L. D. a. D. D. C. Joblin, «Infrared spectroscopy of gas-phase PAH molecules. II. Role of the temperature,» *Astronomy and Astrophysics*, 299, p. 835, 1995.
- [14] G. A. G. J. K. L. J. A. a. F. A. M. F. Salama, «Polycyclic Aromatic Hydrocarbons and the Diffuse Interstellar Bands: A Survey,» *The Astrophysical Journal*, 526(1), p. 265, 1999.
- [15] D. R. W. a. R. J. S. H.-S. Kim, «Single Photon Infrared Emission Spectroscopy of the Gas Phase Pyrene Cation: Support for a Polycyclic Aromatic Hydrocarbon Origin of the Unidentified Infrared

- Emission Bands,» *Physical Review Letters*, 86(25), pp. 5691-5694, 2001.
- [16] G. M. a. C. J. G. Mallocci, «Electronic absorption spectra of PAHs up to vacuum UV. Towards a detailed model of interstellar PAH photophysics,» *Astronomy and Astrophysics*, 426, pp. 105-117, 2004.
- [17] A. B. G. M. G. M. D. T. a. C. J. F. Useli-Bacchitta, «Visible photodissociation spectroscopy of PAH cations and derivatives in the PIRENEA experiment.,» *Chemical Physics*, 37, pp. 16-23, 2010.
- [18] G. M. A. B. a. C. J. Junfeng Zhen, «An optical spectrum of a large isolated gas-phase PAH cation: C78h26,» *Molecular Astrophysics*, 2, pp. 12-17, 2016.
- [19] F. U.-B. H. S. V. B. A. B. P. M. M. a. C. J. Brandi West, «Photodissociation of Pyrene Cations: Structure and Energetics from C16h10+ to C14+ and Almost Everything in Between,» *The Journal of Physical Chemistry A*, 118(36), pp. 7824-7831, 2014.
- [20] S. R. C. C. J. G. M. H. S. A. G. L. N. S. M. J.-P. C. a. P. M. M. Junfeng Zhen, «VUV Photo-processing of PAH Cations: Quantitative Study on the Ionization versus Fragmentation Processes,» *The Astrophysical Journal*, 822(2), p. 113, 2016.
- [21] M. F. C. P. E. P. E. S. J. Z. N. K. R.-H. K. R. W. A. V. a. H. A. M. K. Olof Johansson, «Photoionization Efficiencies of Five Polycyclic Aromatic Hydrocarbons,» *The Journal of Physical Chemistry A*, 121(23), pp. 4447-4454, 2017.
- [22] J. B. R. B. B. C. C. J. M. J. C. O. a. L. C. S. Martin, «Fast Radiative Cooling of Anthracene Observed in a Compact Electrostatic Storage Ring,» *Physical Review Letters*, 110(6), p. 063003, 2013.
- [23] S. B. R. H. A. G. G. M. T. a. T. S. J. Postma, «Ionization and Fragmentation of Anthracene upon Interaction with keV Protons and Particles,» *The Astrophysical Journal*, 708(1), p. 435, 2010.
- [24] H. a. B. J. H. C. a. H. Z. A. I. S. Holm, «Dissociation and multiple ionization energies for five polycyclic aromatic hydrocarbon molecules,» *The Journal of Chemical Physics*, 134(4);, p. 044301, 2011.
- [25] M. A. F. M. a. S. D.-T. Chiara Paris, «Multiple ionization and hydrogen loss from neutral and positively-charged coronene,» *The Journal of Chemical Physics*, 140(20), p. 201307, 2014.
- [26] C. J. a. G. Mulas, «Interstellar polycyclic aromatic hydrocarbons: from space to the laboratory,» *EAS Publications Series*, 35, pp. 133-152, 2009.
- [27] A. G. G. M. Tielens, «Diffuse Interstellar Bands: The Way Forward,» *Proceedings of the International Astronomical Union*, 9(S297), pp. 399-411, 2013.
- [28] A. H. P. R. M. C. R. M. S. M. F. S. H. J. S. R. H. S. H. Z. B. M. L. A. H. C. a. B. H. A. Ławicki.
- [29] Biswas, *Scientific Reports volume 7*, 2017.
- [30] A. P. Moretto-Capelle, 2006.
- [31] J. H. Paul, *At. Data Nucl. Data Tables*, vol. 42,, pp. 105-156, 1989.
- [32] H. W. Hink, *Phys. Rev. A* 4, p. 507, 1971.
- [33] P. G. M. B. B. Deconihout, *Appl. Surf. Sci.* 94/5, p. 442, 1996.
- [34] J. P. a. B. N. A. L. Bennani, «Measurement of the absolute electron detection efficiency of a channel multiplier (channeltron),» *Journal of Physics E: Scientific Instruments*, 6(11), p. 1077, 1973.
- [35] H. J. Blaauw, *J. Phys. B: At. Mol. Phys.* 10, p. 299, 1977.
- [36] N. Y. Itikawa, «Cross sections for electron collision with water molecules,» *J. Phys and Chem Reference Data* 34, p. 1, 2008.

- [37] I. P. R.A. Abrines, *Proc. Phys. Soc.* 88, pp. 861-873, 1966.
- [38] A. S. R.E. Olson, *R.E. Olson and A. Salop, Phys. Rev. A* 16, p. 531, 1977.
- [39] R.E.Olson, *Olson J.Phys.B* 15 , pp. 163-167, 1982.
- [40] I.Abbas, *I. Abbas et al, Phys. Med. Biol.* 53, p. 41, 2008.
- [41] B. W.H.Press, *Numerical Recipies*, Cambridge University Press, 1986.
- [42] T. M.Matsumoto, «Mersenne twister: A 623-dimensionally equidistributed uniform pseudorandom number generator,» *ACM Trans. dans Modeling and Computer Simulations,,* 1998.
- [43] K. J. S. M. J. S. N. K. S. T. M. J. M.W.Schmidt, «"General Atomic and Molecular Electronic Structure System",» *J. Comput. Chem.,* 14, , pp. 1347-1363(1993), 1993.
- [44] M.E.Rudd, *Phys.Rev.A* 28, 1983.
- [45] Verstraete, *Astronomy and Astrophysics* 234, pp. 436-444, 1990.
- [46] M. E. R. G. B. Crooks, «Experimental Evidence for the Mechanism of Charge Transfer into Continuum States,» *Phys. Rev. Lett.* 25, p. 159, 1970.
- [47] M.E.Rudd, «Ionization by low and intermediate energy ion and neutral beams,» *IEEE Transaction on Nuclear Science, NS-28,,* pp. 1135-1138, 1981.
- [48] M. E. Rudd, «Mechanisms of Electron Production in Ion-Atom Collisions,» *Radiation Research, Vol. 64,* pp. 153-180, 1975.
- [49] H. M. C.Champion, «Theoretical predictions for ionization cross sections of DNA nucleobases impacted by light ions,» *Phys. Med. Biol.*55, pp. 6053-6067, 2010.

